SCIENTIFIC REPORTS

OPEN

Received: 30 November 2014
Accepted: 12 May 2015
Published: 05 June 2015

Varied Probability of Staying Collapsed/Extended at the Conformational Equilibrium of Monomeric $A\beta_{40}$ and $A\beta_{42}$

Wanling Song[1], Yuanyuan Wang[1], Jacques-Philippe Colletier[2,3,4], Huaiyu Yang[1] & Yechun Xu[1]

In present study, we set out to investigate the conformation dynamics of $A\beta_{40}$ and $A\beta_{42}$ through exploring the impact of intra-molecular interactions on conformation dynamics using equilibrium molecular dynamics simulations. Our 40 microsecond-scale simulations reveal heterogeneous conformation ensembles of $A\beta_{40}$ and $A\beta_{42}$ that encompass ~35% β-strand and ~60% unstructured coils. Two conformational states were identified in both alloforms: a collapsed state (CS) that resembles the structural motif of face-to-face hydrophobic clustering in amyloid fibrils, and an extended state (ES) that features the structural characteristics of anti-parallel β-sheets in amyloid oligomers. In $A\beta_{40}$, the C-terminus remains unstructured and rarely interacts with other parts, thereof the hydrophobic clustering is in loose contact and the peptide assumes ES with high probability. In contrast, the C-terminus of $A\beta_{42}$ adopts a β-strand structure that strongly interacts with segments E3-R5 and V18-A21. The active association leads to a more compact hydrophobic collapse and refrain the alloform from ES. Based on the structural characterization, we propose that the fibril and oligomer assembly pathways could respectively take off from CS and ES, and their aggregation propensity may be governed by the probability of visiting the corresponding conformational states at the equilibrium.

Alzheimer's disease (AD) is the most frequent cause of senile dementia. The two histological hallmarks of the disease are the appearance of extracellular senile plaques and intracellular neurofibrillary tangles in victims' brains[1–3]. The principal constituent of the plaques is the β-amyloid peptides (Aβs) produced by sequential action of β- and γ-secretases on the amyloid precursor protein (APP)[4,5]. $A\beta_{40}$ and $A\beta_{42}$ are the two most abundant Aβ isoforms in the plaques, with the only difference found at the C-terminus where the latter has two more hydrophobic residues (I41 and A42). It was demonstrated that $A\beta_{42}$ is more neurotoxic than $A\beta_{40}$[6–8] and an increased $A\beta_{42}/A\beta_{40}$ concentration ratio correlates with the onset of AD[9]. The increased neurotoxicity of $A\beta_{42}$ has been proposed to stem from its significantly higher aggregation propensity[10–12]. The molecular basis for this phenomenon remains unclear but likely originates from differences in the conformation dynamics of the two peptides.

$A\beta_{40}$ and $A\beta_{42}$ form β-sheet-containing structures that assemble into a variety of polymorphic oligomers and fibres. Solid-state NMR showed that they both adopt similar U-bent β-sheet rich structures in protofilaments, wherein side chains of residues of the central hydrophobic cluster (CHC, L17-A21) contact those of the C-terminal hydrophobic region (A30-A42)[13,14]. Apart from sharing a U-turn at E22-K28, specific intra- and inter-molecular interactions, however, differ within and between the $A\beta_{40}$ and $A\beta_{42}$ protofilaments[13–16]. X-ray microcrystallography provided atomic-resolution insights into the

[1]CAS Key Laboratory of Receptor Research, Drug Discovery and Design Center, Shanghai Institute of Materia Medica, Chinese Academy of Sciences (CAS), Shanghai 201203, China. [2]Univ. Grenoble Alpes, IBS, F-38044 Grenoble, France. [3]CNRS, IBS, F-38044 Grenoble, France. [4]CEA, IBS, F-38044 Grenoble, France. Correspondence and requests for materials should be addressed to Y.X. (email: ycxu@simm.ac.cn)

structures of Aβ fibre-prone segments, uncovering the molecular basis for Aβ fibre polymorphism[17]. By combining atomic structures with previous nuclear magnetic resonance[13,17,18] and cryo-EM studies[16], several models were constructed for Aβ fibres[19,20].

In contrast to the well-resolved protofilaments, our understanding to structures of the monomeric $A\beta_{40}$ and $A\beta_{42}$ is limited. High-resolution data under physiological conditions are absent, due to the pronounced aggregation propensity and hydrophobicity of Aβ. Instead, much information, regarding the secondary structures, long-range contacts and flexibilities, are gathered by NMR based on various Aβ fragments with improved solubility or in more hydrophobic conditions[12,21–27]. For example, in water, $A\beta_{21-30}$ takes a bended structure with a β-turn at V24-L28[28]; $A\beta_{10-35}$ folds into a collapsed coil where Y10-H14 and V24-N27 condense around the CHC region (L17-A21) in extended structures[24]. In aqueous sodium-dodecyl sulphate (SDS) micelles, which is supposed to simulate the water-membrane environment after γ-secretase intra-membrane action, residues Q15-V36 of $A\beta_{40}$ take on a helical conformation with a hinge a residues G25-N27, while D1-H14 adopt unstructured, extended conformations[29].

Characterizing the conformation dynamics of monomeric $A\beta_{40}$ and $A\beta_{42}$ is a pre-requisite to comprehending the Aβ self-assemble pathway and the differences between the two peptides. The demand on the structural information of full-length Aβ has encouraged the application of molecular dynamics (MD) simulations. Enhanced sampling methods were developed to explore the highly diverse conformational ensembles accessible to Aβs[30–32]. Several noteworthy studies include that Vitalis *et al.* conducted multiple replica-exchange Monte Carlo simulations with implicit solvent model, from which a micelle-like architecture of Aβs monomers was revealed[33]; Sgourakis *et al.* and Ball *et al.* respectively performed replica-exchange molecular dynamics simulations in conjunction with NMR data and confirmed the existence of structured region in these two intrinsically disordered peptides[30,34,35]; more recently, Lin *et al.* deployed Markov state model analysis based on extensive *in silico* samplings and observed reduced β-hairpin formation near C-terminus of the shorter Aβ monomer[36]. Admittedly, the structures of Aβs monomers have been probed by several computational studies and a further one of such may seem difficult to justify at first sight. However, the structural differences between $A\beta_{40}$ and $A\beta_{42}$ revealed so far appear surprisingly trivia in comparison to the apparent gaps in their aggregation propensity. In fact, most *in silico* studies that succeeded in discriminating the two alloforms remained equivocal in interpreting the structural information in terms of understanding Aβ aggregation. This predicament comes from two points: i/ the force field bias and ii/ the complexity of Aβ conformational space. While the former contributes to significant lower content of β-sheet (~6%–7%) in comparison to the estimation from CD experiments (~30%)[37] and may lead to biased samplings[38], the latter requires such large volumes of samplings for a generalized understanding that may go beyond our current computation limits. Thus, characterizing the conformation dynamics and understanding the structural differences of Aβs call for alternative ways.

In current study, we set out to investigate the impact of intra-molecular interactions on the dynamics of Aβs using equilibrium MD simulations and an atomistic force field from Gromos family (Gromos 53a6 ff). We implemented 40 microsecond-scale molecular dynamics simulations on $A\beta_{40}$ and $A\beta_{42}$ (70.6 μs in aggregate simulation time), allowing unprecedented insights into their equilibrium dynamics. The simulation data showed improved consistency with three-bond J-coupling constants and residual dipolar couplings than previous works. The secondary structure profiles from our simulations that comprise of ~35% in β-strand and ~60% as random coils are also in better agreement with CD estimations. Spectral clustering revealed that both isoforms exists in two states: i/ a collapsed state (CS) held together through hydrophobic clustering; and ii/ an extended state (ES) populated with higher orders of β-strands. The C-terminal β-hairpin of $A\beta_{42}$ diminishes the overall conformational entropy via stabilizing the peptide in the collapsed state. In contrast, the C-terminus of $A\beta_{40}$ only shows weak intra-molecular interactions. The shorter peptide, hence, enjoys more efficient transition to the extended state. The resemblance of CS to amyloid fibril and ES to the observed oligomers indicates that they respectively could be the starting point of fibril and oligomer assembly pathways. Our results thus suggest that the aggregation propensity of amyloid peptides may be encoded in the probability of adopting the corresponding conformational states at the equilibrium.

Results

Validation and characterization of the conformation ensembles. Two sets of simulations were generated for both $A\beta_{40}$ and $A\beta_{42}$, each containing ten trajectories (Table 1). In the first set of simulations (Group A and C for $A\beta_{40}$ and $A\beta_{42}$, respectively), the starting models were taken from the coil structure of $A\beta_{10-35}$ in water with necessary residues added manually[24]. The second set of simulations (Group B and D for $A\beta_{40}$ and $A\beta_{42}$, respectively) was based on the helical structure of $A\beta_{40}$ in SDS micelles[29]. Using two NMR structures of monomeric Aβ allows diversifying our conformational sampling while reducing the starting model bias during the simulations. Groups from the same structural set were extended to similar lengths, while to account for the time required for helix unreeling, the helix-starting set were systematically run longer than the other. In the first 200 ns of simulations, large structural changes occur in both $A\beta_{40}$ and $A\beta_{42}$ (Fig. S1), thus corresponding data were discarded. Using a conformation-saving interval of 100 ps, the resulting number of sampling points are 154,481, 176,112, 154,392 and 187,712 in Group A, B, C and D, respectively.

Group	PDB code	Peptide	Trajectory	Length (μs)	Group	PDB code	Peptide	Trajectory	Length μs
A	1hz3 (Coils)	$A\beta_{40}$	A1	1.7	**B**	1ba4 (Helices)	$A\beta_{40}$	B1	1.9
			A2	2.0				B2	1.7
			A3	1.8				B3	3.3
			A4	1.1				B4	2.3
			A5	1.1				B5	1.8
			A6	2.8				B6	1.7
			A7	1.3				B7	1.0
			A8	1.1				B8	1.6
			A9	1.2				B9	1.0
			A10	1.9				B10	2.8
C	1hz3 (Coils)	$A\beta_{42}$	C5	1.8	**D**	1ba4 (Helices)	$A\beta_{42}$	D1	2.0
			C2	2.0				D2	1.8
			C3	1.6				D3	2.1
			C4	2.1				D4	2.0
			C5	1.4				D5	2.1
			C6	1.2				D6	2.8
			C7	1.3				D7	1.2
			C8	2.2				D8	1.7
			C9	1.4				D9	2.7
			C10	1.7				D10	2.1

Table 1. Configuration of the simulations.

Validation of the samplings was made through comparisons of the back-calculated three-bond J-coupling constant ${}^3J_{H^N H^\alpha}$ and residual dipole couplings (RDCs) with the experimental measurements from Yan *et al.*[39]. We examined different parameter sets for the Karplus equation in calculating J-coupling as described in Method. In general, good consistency was observed between the experimental and back-calculated data. The RMSD in the best-fitting set (Fig. 1A) is ~0.78 Hz for $A\beta_{40}$ and ~0.82 Hz for $A\beta_{42}$. The result is lower than or comparable to those using other force fields[30,34,35]. Residues Q15, A21 and A30 in $A\beta_{40}$, and A21 in $A\beta_{42}$ exhibit the largest deviation. These residues locate at two different sets of complex environment: Q15 at a very flexible region with multiple charges and A21/A30 at hydrophobic patches with charged residues at vicinity. That these outliners are also observed in previous simulations may reflect some common limitations among modern force fields in taking care of the interplay of multiple factors. Residual dipole coupling constants were calculated by PALES[40] using global alignment. The RDCs are in excellent agreement with the experimental data, showing an average RMSD of ~1.06 Hz for $A\beta_{40}$ and ~1.16 Hz for $A\beta_{42}$ (Fig. 1B). The Pearson's correlation coefficient (P.C.C) reaches above 0.75 for all groups, which is a significant improvement from previous simulations. Residues on flexible loops, including V12, K16 and L17 in $A\beta_{40}$ and Q15 in $A\beta_{42}$, exhibit the largest deviation. The discrepancy may result from the intrinsic uncertainty of backbone orientation of the flexible loop. Taken together, the good agreement with the NMR measurements indicates that our simulations have sampled the correct conformational shapes of $A\beta_{40}$ and $A\beta_{42}$.

The secondary structure occupancy by residue was calculated using DSSP[41]. In accordance with the solution NMR analyses, the difference between the two alloforms is subtle. The two peptides share three regions with the highest propensity of forming β-strands, locating at E3-R5, L17-A21 and I31-M35, and in-between regions of turns and bends centring at D7-G9, H13-Q15 and V24-N27 (Fig. 2). The charged residues at the turns and bends form several most stable hydrogen bonds in both peptides, including D7 with S8, H14 with K16, and E22/D23 with S26/N27-K28, while other steady hydrogen bonds are observed between adjacent contacts, e.g. E3 with R5, and E11 with H13 (Fig. S2 and S3). The most striking difference in the secondary structures of the two peptides lies at the C-terminus, in agreement with NMR findings[21]. In $A\beta_{42}$, residues V39-A42 folds into an additional, extremely resilient β-strand, whereas its counterpart in the shorter alloform (G37-V40) remains largely unstructured.

The content of secondary structure elements was also calculated. According to the group-averaged profiles, our samplings of $A\beta_{40}$ and $A\beta_{42}$ are dominated by two sets of structural elements: coil/bend/turn and β-strands, whose occupancies in these two alloforms are similar (Fig. S4 and Table S1). In the coil-starting groups (A and C), the occupancy of coil/bend/turn and β-strand are ~58% and ~41% respectively, while in the helix-starting groups (B and D), they are ~62% and ~36% respectively. The

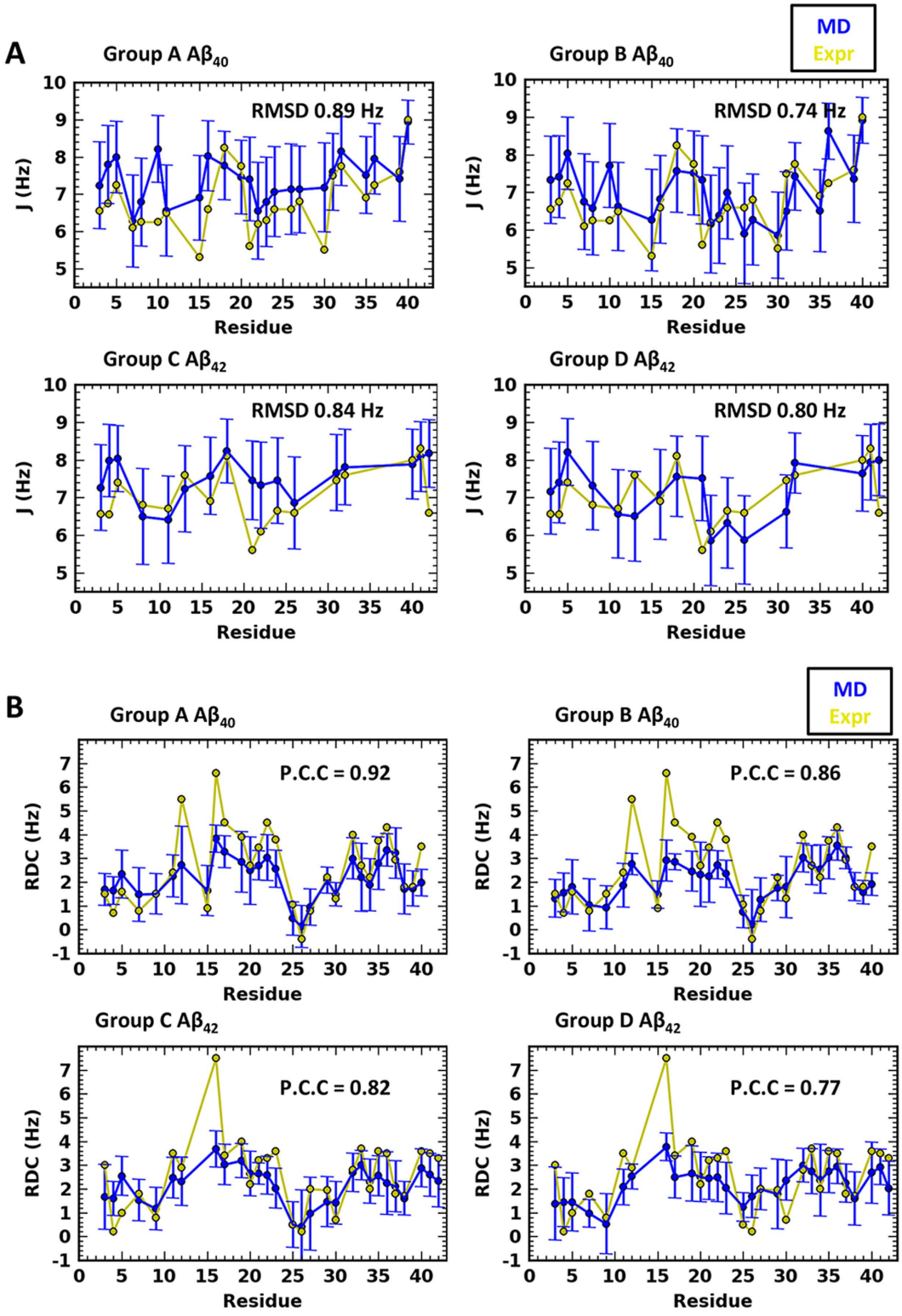

Figure 1. Validation with NMR measurements. The back-calculated J-coupling values (**A**) and residual dipole coupling constants (**B**) from our simulation coordinates are compared with the NMR data from Yan *et al.*[39]. Simulations data are shown in blue circles and experimental data yellow ones. The error bars denote the standard deviations from the 10 trajectories in each simulation group.

helical content is low, remaining at ~1%, whereas a slight increase of the content is observed in the helix-starting groups, due to the unreeling process. Notably, the secondary structure profiles display large discrepancy with those from previous simulations on Aβs that comprised of ~6–7% β-sheet and

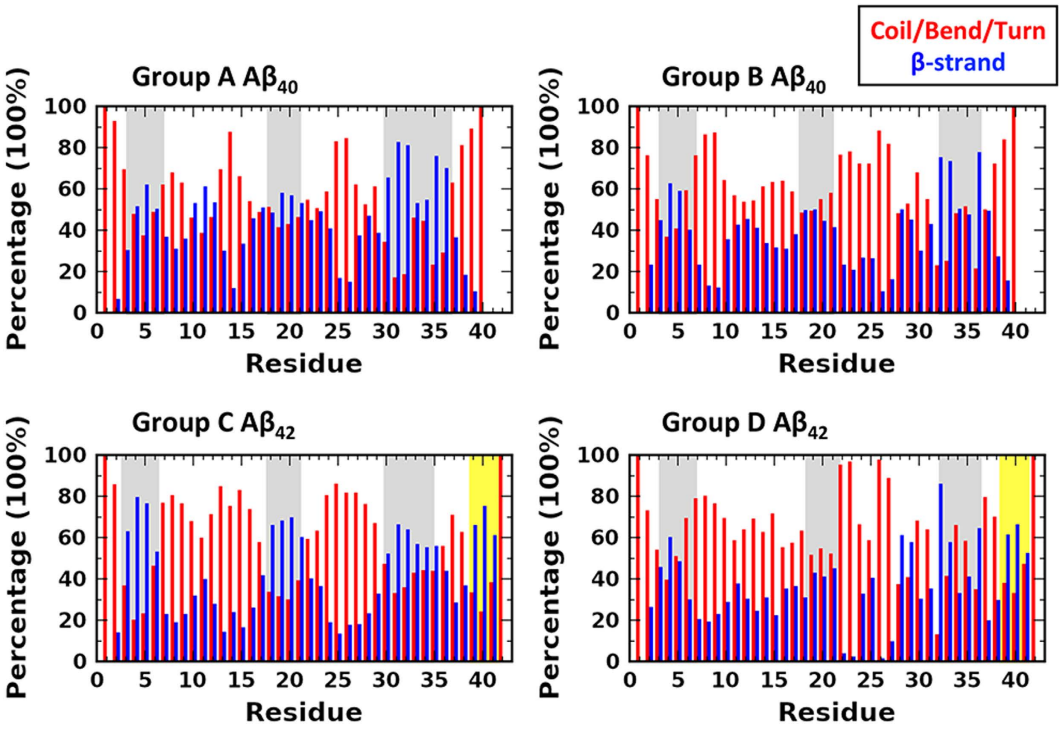

Figure 2. Secondary structure occupancy by residue. Red and blue bins are the percentage of structural elements of coil/bend/turns and β-strand occupying each residue, respectively. The β-strand regions shared by four groups are highlighted in gray, and the extra β-strand in $A\beta_{42}$ is in yellow.

~20–30% helix[30,34]. But the data from the present simulations are indeed in better consistency with the CD spectroscopy results that reveal the two alloforms containing ~30% β-strand and 5% helix[37,42]. Thereof, our simulations, in conjunction with the experiments, suggest that higher content of β-strand presents in Aβ monomers than the calculation from previous simulations, and accordingly raise questions about the hypothesis that the rate-limiting step of amyloid aggregation lies in the transition to conformations with higher β-strand-content at monomer level.

Two conformational states in $A\beta_{40}$ and $A\beta_{42}$. A spectral clustering approach designed by Sgourakis *et al.*[35] were used to characterize the conformational states in each group. This clustering approach is based on pair-wise contact information rather than the calculation of RMSD, and is advised in the studies on small intrinsically disordered peptides like Aβs, which experience drastic changes in molecular shapes during simulations and depower clustering strategies based on geometry distance. Following the procedures introduced in the paper, we obtained a small number of eigenvectors that can be used to cluster the conformations into groups that share interaction patterns. A direct visualization of the conformations in the space defined by the three most discriminative eigenvectors is shown in Fig. S5. Each group of conformation ensembles were clustered into ten interaction patterns (See Methods for the discussion on the cluster numbers), and the conformations at the centroid of all clusters are reported in Fig. S6-S9.

The 40 representative conformations showed high heterogeneity in loop and β-sheet arrangements, recapitulating conformational heterogeneity from experiments. We observed two dominant conformational states in $A\beta_{40}$ and $A\beta_{42}$: a collapsed state (CS) and an extended state (ES), although the specific residue-residue associations differ among clusters from the two alloforms. A couple of typical conformations in each state are shown in Fig. 3. In the CS, hydrophobic residues, most frequently including F4, V18, F20, A21, I31, L34 and V36, collapse into a core that forms the base of a highly dynamic globule at the surface of which polar and charged residues stand facing the solvent. The collapse contributes a main stabilizing factor to the state, while also gives rise to the dynamics, *i.e.* the disordered state, of the conformations. A variety of residue associations are observed in both alloforms. In $A\beta_{40}$, the hydrophobic collapse can involve β-strands V18-A21/A30-L34 and loop F4-D7 (Fig. 3B), or β-strands Y10-H13/V18-A21 and loops F4-D7/G29-I32/M35-G37 (Fig. 3A). In $A\beta_{42}$, the participants can be grouped into two sets: one involving two β-sheets formed by G38-I41/V18-A21, and A30-G33/G9-V12 (Fig. 3G,H), while the other two β-sheets by V39-I41/E3-R5, and L17-A21/K28-L34 (Fig. 3I). Apart from the hydrophobic stacking, polar contacts also play an important role in maintaining the conformations. The conserved interactions of H6-S8 and V24-K28 stabilize the required turns/loops that bring distal hydrophobic patches in vicinity.

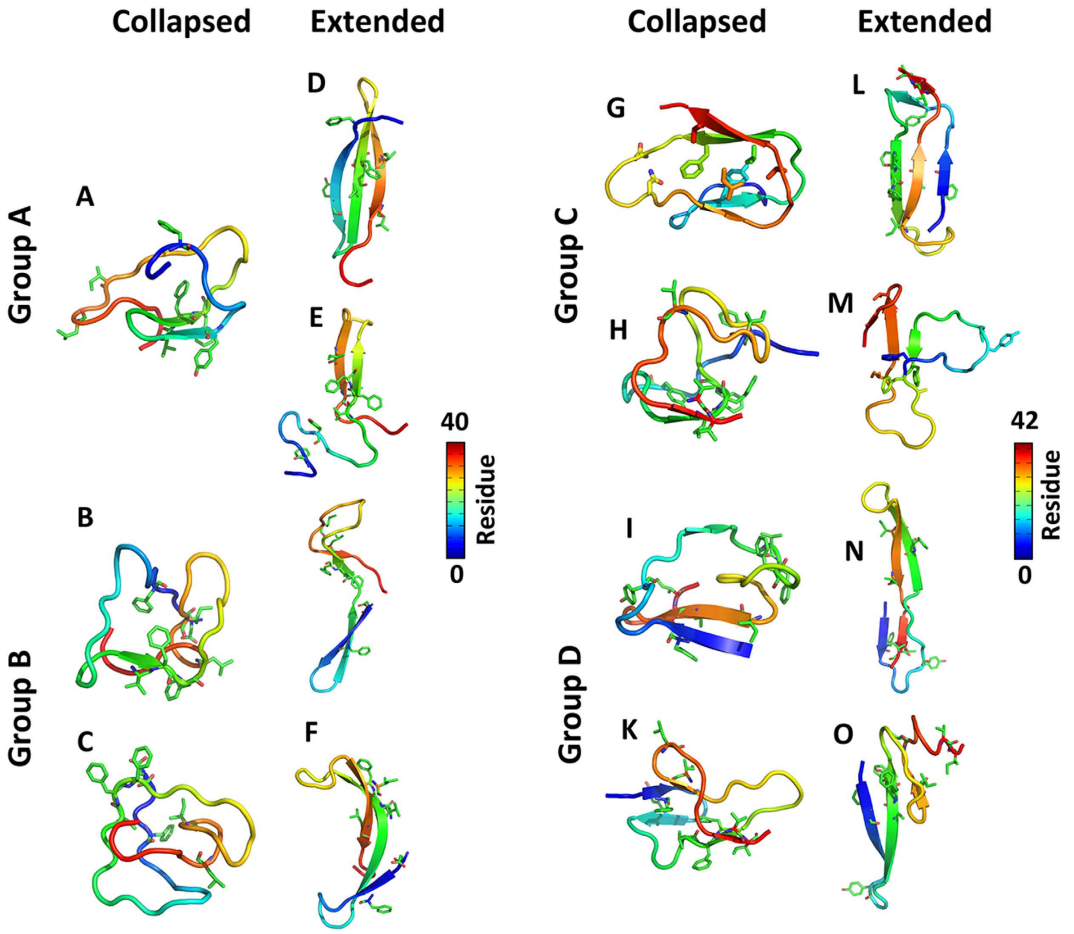

Figure 3. The typical collapsed and extended conformations in $A\beta_{40}$ and $A\beta_{42}$. Peptides are colored in rainbow based on Cα atoms. The hydrophobic residues that are frequently observed in the hydrophobic clustering, including F4, Y10, V12, F19, F20, A21, I31, L34, and V36, are shown in sticks.

The CS revealed by our samplings share similarities with the micelle-like conformations reported by Vitalis *et al.*[33] in that hydrophobic residues collapse into a dynamics core. But three major differences come up under closer comparison. Firstly, higher content of β-strand is revealed in our samplings. In particular, the N-terminal regions of both $A\beta_{40}$ and $A\beta_{42}$ are frequently occupied by β-strand in our simulations, and more active in intra-molecular associations with other parts of the peptide. An entirely unstructured and unpaired N-terminus as proposed by Vitalis, we suggested that, is not very likely, since this region populates multiple charged residues that are capable of forming polar contact with the rest of the peptides (Fig. S2 and S3). Plus, a structured N-terminus is also supported by the ^{1}H NMR data from Danielsson *et al.* that provide evidence of $A\beta_{40}$ N-terminus taking β-strand conformation at room temperature[43]. Secondly, other than entirely collapsed coils, the CSs in our samplings prefer a roll shape in which hydrophobic residues contact the solvent at two flanks. Such an arrangement is reminiscent of the monomer structure in amyloid fibril. In particular, the two β-strands in the fibril constructs, *i.e.* V18-A21 and A30-M35, are frequently involved in the hydrophobic collapse of both alloforms. Thirdly, distinct structural differences between $A\beta_{40}$ and $A\beta_{42}$ are observed. In $A\beta_{40}$, the present of loops in the hydrophobic collapse brings in flexibility and leads to loose internal structures in the conformations. In comparison, the CS of $A\beta_{42}$ has a more structured collapse that results in compact conformations and reduced solvent exposure of hydrophobic residues. As shown by the solvent accessible surface area (SASA) of the hydrophobic residues (Fig. 4A), typical CS conformations are observed below 550 $Å^2$ in both alloforms. But the conformations in $A\beta_{42}$ on average exhibit significant lower SASA than those in the shorter alloform.

In the ES, the hydrophobic core breaks down, and Aβ adopts more flattened shapes where the main interactions are replaced by hydrogen bonds between β-strands. ES containing two to six antiparallel β-strands are observed, several of which reproduce the characteristics of experimentally determined Aβ oligomer structures. Notably, Cluster 9 of Group A ($A\beta_{40}$) that comprises of two anti-parallel β-strands at V18-E22 and A30-M35 (Fig. 3E) show high similarity to the β-hairpin of $A\beta_{40}$ stabilized by an affibody (PDB code 2OTK)[44]. The Cα RMSD between the NMR structure and the best-fitting from the cluster

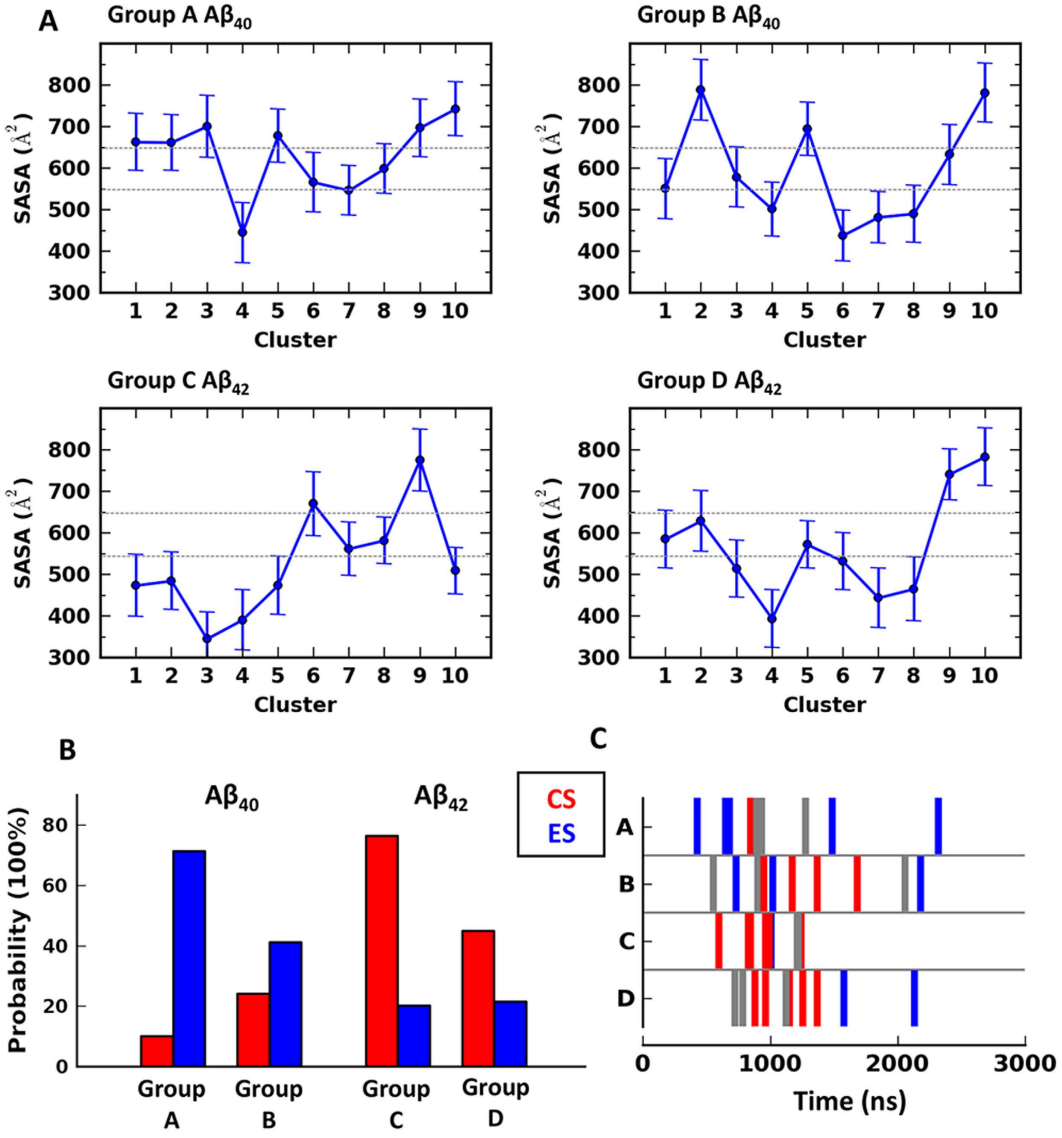

Figure 4. Varied distribution of collapsed/extended states in $A\beta_{40}$ and $A\beta_{42}$. **A**) The solvent accessible surface area (SASA) of the residues that are most frequently observed in the hydrophobic collapse of both alloforms, *i.e.* F4, V18, F20, A21, I31, L34 and V36. The SASA is averaged from all the snapshots in each cluster. The error bars denote standard deviation within the cluster. **B**) The probability of observing collapsed/extended states in each group. The collapsed state is defined as SASA below 550 Å^2, and the extended state as SASA above 650 Å^2. **C**) The average appearance time of each cluster in the course of simulations. The clusters in collapsed state are colored red and in extenddd state colored blue. Those between the two states, *i.e.* SASA between 550 Å^2 and 650 Å^2, are in gray.

is 0.4 Å (Fig. 5). Apart from the NMR determined part, conformations in this cluster also have a short N-terminal hairpin (E3-H6 and Y10-V12) that is connected to the other end through a loop at H13-L17. The flexibility of H13-L17 may correspond to the unobservable NOEs and the NMR chemical shifts that are close to random coil values in the N-terminal region[44]. Cluster 6 of Group C ($A\beta_{42}$) matches the β-meander structure proposed for an $A\beta_{42}$ pentamer oligomer by Ahmed *et al.*[45]. In agreement with the solid-state NMR results, conformations in this cluster compose of three anti-parallel β-strands of CHC, I31-V36 and V39-I41 connected by a turn at G37-G38 and a loop at D23-K28 (Fig. 3M). The N-terminal is in unstructured loop, which is consistent with the experimental observation that the amide hydrogen-deuterium exchange rate is high in this region[45]. Other frequent ES conformations include structures of three β-strands that are contributed by F4-S8, Q15-A21 and G29-V36 in $A\beta_{40}$ (Fig. 3D) and residues A2-H6, V18-E22 and G37-I41 in $A\beta_{42}$ (Fig. 3L).

$A\beta_{40}$ and $A\beta_{42}$ show varied probabilities of staying CS/ES. We next set out to calculate the probability of finding CS/ES in each simulation group. Solvent accessible surface area (SASA) of hydrophobic

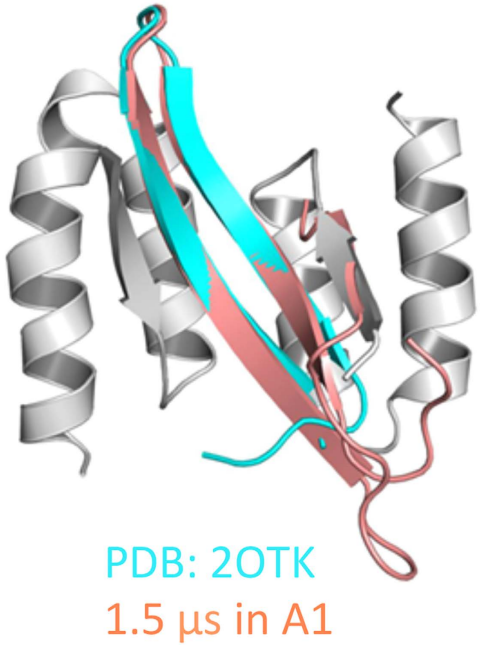

Figure 5. Superposition of the best-fitting ES conformation (salmon) to the NMR structure of $A\beta_{40}$ in complex with an affibody (PDB code 2OTK) (cyan). The best-fitting conformation is from Cluster 9 of Group A. The affibody in the NMR structure is colored gray.

residues was used to define the two conformational states. Typical collapsed conformations are found below SASA = 550 Å^2 and typical extended above 650 Å^2 (Fig. 4A). Based on this criteria, the probability of $A\beta_{40}$ staying in CS/ES is ~10%/71% and ~24%/41% in Group A and B respectively, whereas that of $A\beta_{42}$ is ~76%/20% and 44%/21% in Group C and D respectively (Fig. 4B). Striking difference exists between the two allforms and the longer one shows obvious preference to staying in CS. To investigate the transition between CS and ES in the two alloforms, we further calculated the appearance of the two conformational states in the course of simulations. In the coil-starting groups, the first three clusters of $A\beta_{40}$ belong to ES conformations with an average appearance ranging from 500 ns to 800 ns, indicating that the shorter alloform is able to efficiently take extended conformations from coils. The sole CS cluster of $A\beta_{40}$ in the group has an average appearance of ~900 ns. $A\beta_{42}$ from the similar starting configurations, however, exhibits a very different scenario. The first five clusters in the group are in CS conformations, showing an average appearance between 600 ns and 1000 ns, whereas the mere two ES clusters lie at ~950 ns and ~1200 ns respectively (Fig. 4C). The predominance suggests that the longer alloform prefers to adopt CS from coils. In the helix-starting groups, an unreeling event first takes place that gives rises to larger proportion of conformations whose SASA is between 550-650 Å^2 (gray bars in Fig. 4C), and postpones the CS and ES. Nevertheless, the trend is similar to that in the coil-starting groups. During the unreeling, the C-terminal β-strand of $A\beta_{42}$ are able to frequently associate with N-terminus, and create a beneficial environment that fosters hydrophobic clustering. Thus the first CS cluster in Group D averages at ~750 ns (Cluster 3), long before the two ES clusters that lie at ~1500 ns and ~2100 ns. In contrast, the unstructured C-terminus of $A\beta_{40}$ shows significantly decreased interaction with other parts of the peptide. This leads to that the peptide is less efficient in organizing a hydrophobic collapse and in some case directly transit into ES. Thereof, the first ES in Group B (~750 ns) advances the first CS cluster (~990 ns).

The role of the C-terminal β-strand in $A\beta_{42}$. The mere difference between $A\beta_{40}$ and $A\beta_{42}$, in the aspect of sequence, is the presence of two extra hydrophobic residues at the C-terminus of the latter. In line with experimental observations and previous simulations[21,27,30,36,44], the additional two hydrophobic residues contribute to an extremely resilient β-strand in our obtained conformation ensembles of $A\beta_{42}$ (Fig. 2). As a result, the β-strands in the rest of $A\beta_{42}$ shift by residues in comparison to the shorter one, and the intra-molecular associations are altered. In $A\beta_{40}$, the most frequent interactions are found between A2-H6 and Y10-H14, and between H14-F20 and A30-V36. But in $A\beta_{42}$, as the C-terminus shows high preference to form β-sheet with E3-R5 or V18-A21, the frequent associations are instead found between V18-D23 and K28-G33 (Fig. 6). The altered associations lead to two major changes in the conformation and dynamics of $A\beta_{42}$. Firstly, the active interaction of the C-terminal β-strand with the rest of the peptide brings C-terminal hydrophobic region and CHC region in vicinity, which creates beneficial environment that fosters the hydrophobic collapse formation. Indeed, the transition to CS is efficient in both coil- and helix-starting simulations of $A\beta_{42}$. Plus, when the longer alloform is taking the

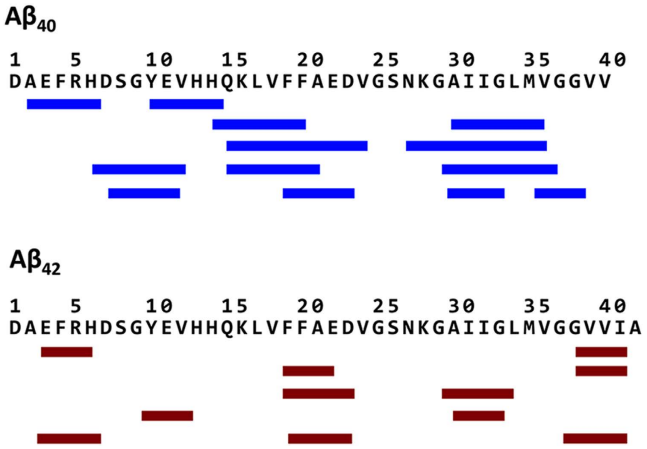

Figure 6. β-sheet associations. The major β-sheet associations observed in the conformation ensembles of $A\beta_{40}$ and $A\beta_{42}$ are labelled by strips and paired by lines.

ES, the extra β-strand also bends conformations through its intra-molecular associations. The bended shape prevents the β-strands from further elongation, and restrains the hydrophobic residues from further breaking. As a result, the transition is reversible, and the peptide is capable of returning to the CS, though less compact, after having folded into the ES (Fig. S10). Secondly, the C-terminal β-strand brings in the $A\beta_{42}$ hydrophobic collapse higher content of β-sheet associations, the main-chain hydrogen bonds of which 'strip seal' the conformations. One apparent outcome of such structures is that the stability of CS is increased and the appearance of ES is delayed. In comparison, the unpaired C-terminus of $A\beta_{40}$ significantly weakens the hydrophobic collapse, as the C-terminal hydrophobic residues are impeded from active involvement in the collapse and the resulting CS has less local structures. In addition, the conformational constrain imposed by the association of C-terminus with the rest of $A\beta_{42}$ in ES is also relieved in $A\beta_{40}$. The shorter alloform is able to arrange the β-strands in ES in flat tandem and easily expand into longer lengths (Fig. S10).

Discussion

By performing 40 equilibrium MD simulations, we sufficiently expore the impact of intra-molecular interactions on conformation dynamics. The obtained conformations exhibit improved consistency with NMR measurements than previous simulations. The P.C.C between RDC values back-calculted from our coordinates and measurements from NMR reaches above 0.75, whereas previous ones show a range of 0.4–0.5[30,34,35,46]. The improvement is ascribed to better sampling of β-strand. We observed ~35% β-strand alongside ~60% unstructured coils, which is in good congruency with CD estimation from Fezoui *et al.*[37]. In fact, this trend has already appeared in the simulations adopting REMD method. From Sgourakis *et al.*[35] to Rosenman *et al.*[47], an increased agreement with NMR measurements is accompanied by samplings with more β-strands at local regions. The notion of extended structures occupying local regions also gains supports from experiments. Through two-dimensional NMR, Hou *et al.*[25] demonstrate that the two hydrophobic regions on Aβs, *i.e.* the central hydrophobic segment and I31-V36, are occupied by β-strands. Danielsson *et al.*[43], by using ^{1}H NMR spectroscopy, provide conclusive evidence that N-terminal region and central hydrophobic segment are taking β-strand conformations at room temperature. Thus, our simulations, in conjunction with the experimental data, confirm that higher content of β-strand are indeed populated in Aβs than estimations from previous *in silico* studies.

The obtained ensembles capture a couple of distinct conformations that are reveled by several independent sutdies, including the micelle-like conformations by Vitalis *et al.*[33] and the β-pleated structures by Hoyer *et al.*[44] and Rosenman *et al.*[47]. We assign the former conformational state as CS and the latter as ES. As the equilibrium molecular dynamics simulations are able to sample these conformational states within one trajectory, the probability of visiting each state can be calculated. The results reveal that both $A\beta_{40}$ and $A\beta_{42}$ experience transitions between CS and ES. This observation is in line with the NMR readings that the two isoforms share similar R_1, R_2 and nuclear Overhauser enhancement (NOE) values[21]. The longer alloform shows significant higher propensity of staying in CS than the shorter one. The shifted preference results from changes in inter-molecular associations, *i.e.* more compact hydrophobic collapse, and in local conformations, *i.e.* more ordered structures in hydrophobic collapse, all of which can be unequivocally assigned back to the addition of a β-strand at $A\beta_{42}$ C-terminus. The series of related changes brought about by the extra β-strand point out a critical role of residual interactions in shaping the conformation of Aβ, and raise doubts on the biological relevance of Aβ fragments to full-lengths. Thus extra cautions should be made when deducing the full-length structures of Aβs based on the fragments that indeed exhibit very different biophysical properties, such as the solubility and aggregation kinetics, than the former[23,24,26,48].

A tormenting question in understanding amyloid peptide aggregations is why $A\beta_{42}$, with addition of merely two residues, exhibits much pronounced aggregation propensity comparing to $A\beta_{40}$. As plenty of experiments have demonstrated that the amyloid aggregation characterizes as an obvious nucleation-dependent process[49], the pertinent issue in this puzzle may well become why the nucleation in the longer alloform occurs with much higher efficiency than that in the shorter one. Paravastu *et al.* showed that the molecular structure of mature fibrils is closely related to and mostly likely to reflect the structure of seedings[50]. It is thus reasonable to posit that the nucleate of amyloid fibrils should bear some of, if not all, the characteristics of mature fibril structures. The conformations in CS carry distinct face-to-face interactions of hydrophobic patches that resemble the structural motif in fibrils. Several critical interactions in fibrils are also preserved in CS, including the invariant involvement of hydrophobic patches of V18-A21 and I31-M35, and polar contact of V24-L28 at the conserved turn. Plus, from a kinetic point of view, the association of collapsed conformations is beneficial, as the merge of hydrophobic collapses could be rewarded by an entropy gain that results from reducing solvent exposure of hydrophobic residues. Based on these observations, it is tempting to propose that the nucleation takes off from CS and the structural diversity observed in CS corresponds to the differences in fibrillar architectures. As our simulation results demonstrate that the probability of $A\beta_{42}$ staying in CS is significantly higher than $A\beta_{40}$, the enhanced aggregation propensity of the former could result from the consequent lowered energy barrier for nucleate formation. Besides, greater resemblance to fibril structure is observed in the CS of $A\beta_{42}$, including increased occupancy of β-strand at V18-A21 and I31-M35 and compact hydrophobic collapsed. These structural advantages could also contribute to the effectiveness of nucleation.

The ES conformations carry the signature structure of amyloid oligomers, *i.e.* antiparallel β-sheet[51]. Indeed, several clusters resemble the experimentally determined oligomer structures, including the β-hairpin in complex with an affibody by Hoyer *et al.*[44], and the β-meandering in the disc-like pentamer by Ahmed *et al.*[45]. It was posited based on the finding of Hoyer *et al.* that the stacking of β-hairpins would transit into the structural motif of fibrils through a 90° rotation in the axis of backbone. While the intimidating energy barrier challenges such transition, experiments have demonstrated that the nucleates of oligomers do not seed fibril formation out of monomeric Aβs[52]. On the other hand, our simulations suggest that the collapsed state and extended state co-exist in Aβ conformation ensembles. It is thus more likely that nucleates of fibrils and oligomers originate from different monomeric conformations. An appropriate condition induces a particular form of nucleate that determines the consequent structure of fibril or oligomer. If further verified experimentally, the theory of Aβ assembly proposed here would provide valuable understanding and new manipulating methods to amyloid aggregation.

Methods

System setup. The coil-starting and helix-starting conformations were based on NMR structures of $A\beta_{10-35}$ in water (pdb code: 1hz3)[24] and that of $A\beta_{1-40}$ in a water-micelle environment (pdb code: 1ba4)[29]. The first ten models of each PDB entry were used, upon which the rest of residues were added manually in PyMol to create the desired length. Each of the forty generated peptides was then put in centre of a cubic box with box edge 2.0 nm away from the peptide. Each cubic box was solvated with water molecules using simple point charge (SPC) model and neutralized by ions (3 Na^+).

MD simulation. The simulations of the forty Aβ systems were carried out with GROMACS 4.5 package[53], applying GROMOS 53a6 force field on the peptides and solvents[54]. Periodic boundary conditions were used in x, y and z directions. The LINCS method[55] was used to restrain all bonds, allowing a safe integration step of 2 fs. Electrostatic interactions were computed using the Particle Mesh Ewald (PME) method[56]. Lennard-Jones and Coulomb cut-off distances were set to 1.4 nm and 1.2 nm respectively. To energy-minimize the configurations, all simulations were subjected to the same four-step minimization with positional restrains imposed on (i) heavy atoms, (ii) main-chain atoms, (iii) Cα atoms and (iv) no atoms, step-wise. In the end, a maximum force less than 100 $kJ.mol^{-1}.nm^{-1}$ was obtained for each system. Four steps of thermalization in NPT ensemble, each lasting 500 ps, were subsequently implemented. The peptide and the solvent were coupled separately to a V-rescale thermostat[57] at 300 K with positional restrains applied in the same order as that in the energy minimization. The pressure was kept constant at 1 bar by coupling to a berendsen barostat with $\tau_P = 1.0$ ps and a compressibility of 4.6×10^{-5} bar[58]. In the production runs, all parameters were set to the same as the last step of thermalization and the coordinates of the systems were saved every 100 ps. Table 1 lists the lengths of the simulations on Aβs. The simulations in negative control set were carried out for 500 ns.

Back-calculation of J-coupling values and residual dipole constants. The Karplus equation was used to calculate the $3J_{H^N H^a}$ constant from our simulation coordinates[59]: $J = a\ cos^2(\phi - 60^\circ) + b\ cos(\phi - 60^\circ) + c$, where ϕ is the peptide dihedral angle. The experimental J coupling data were obtained from Yan *et al.*[39]. The motional average effects were explicitly taken into account by fitting the Karplus coefficient to experimental data. Various published data sets were explored[35,60–62], the calculated RMSD ranging from 0.7 Hz to 1.5 Hz. The best fitting was observed using parameters reported by Sgourakis *et al.*[35], in which a, b and c are 7.7, −1.9 and 0.06 respectively.

The residual dipole constants from our simulations coordinates were calculated using PALES[40]. Calculation was implemented on snapshots every 1 ns and averaged within trajectories. The correlation between the experimental values obtained by Yan *et al.*[39] and our back-calculated ones was calculated using Pearson correlation coefficient (P.C.C): $P.\ C.\ C = \frac{Cov(X,\ Y)}{\sigma^2(X) * \sigma^2(Y)}$, where $Cov(X,Y)$ is the covariance of the two variables, and $\sigma^2(X)$, $\sigma^2(Y)$ are the standard deviations.

Spectral clustering. To find a small number of representative conformations for our large conformation ensembles, we employed a spectral clustering technique based on contact maps that was introduced by Sgourakis *et al.*[35]. We confirmed a contact when the COMs of two residues main-chains are closer than 4.5 Å, and denotes it as "1"; otherwise, a non-contact as "0". The pair-wise contact information of one conformation then is expressed as a binary vector. The binary matrix that contains the contact information from one simulation group was transformed into square affinity matrix whose elements were the 'distance' between pairs of conformations. Singular value decomposition on the affinity matrix gave out high discriminative eigenvectors that can be used for data clustering and data visualization. We used the seven most discriminative eigenvectors for data clustering and the three most for visualization (Fig. S11).

The k-means/k-medoid method was used during data clustering and implemented by Pycluster module of Python. The within-cluster sum of distance was monitored as a function of cluster numbers. The number of clusters in each group was set after the turning point of the curve of cluster numbers vs. within-cluster sum distance (Fig. S11). Eventually we chose 10 clusters for each group.

References

1. Hardy, J. A. & Higgins, G. A. Alzheimer's disease: the amyloid cascade hypothesis. *Science* **256,** 184–185 (1992).
2. Hardy, J. & Selkoe, D. J. The amyloid hypothesis of Alzheimer's disease: progress and problems on the road to therapeutics. *Science* **297,** 353–356 (2002).
3. Selkoe, D. J. Alzheimer's disease: genes, proteins, and therapy. *Physiol. Rev.* **81,** 741–766 (2001).
4. Esler, W. P. & Wolfe, M. S. A portrait of Alzheimer secretases--new features and familiar faces. *Science* **293,** 1449–1454 (2001).
5. Masters, C. L. *et al.* Amyloid plaque core protein in Alzheimer disease and Down syndrome. *Proc. Natl. Acad. Sci. USA* **82,** 4245–4249 (1985).
6. Klein, W. L., Stine, W. B., Jr. & Teplow, D. B. Small assemblies of unmodified amyloid beta-protein are the proximate neurotoxin in Alzheimer's disease. *Neurobiol. Aging* **25,** 569–580 (2004).
7. El-Agnaf, O. M., Mahil, D. S., Patel, B. P. & Austen, B. M. Oligomerization and toxicity of beta-amyloid-42 implicated in Alzheimer's disease. *Biochem. Biophys. Res. Commun.* **273,** 1003–1007 (2000).
8. Mucke, L. *et al.* High-level neuronal expression of abeta 1-42 in wild-type human amyloid protein precursor transgenic mice: synaptotoxicity without plaque formation. *J. Neurosci.* **20,** 4050–4058 (2000).
9. Suzuki, N. *et al.* An increased percentage of long amyloid beta protein secreted by familial amyloid beta protein precursor (beta APP717) mutants. *Science* **264,** 1336–1340 (1994).
10. Jarrett, J. T., Berger, E. P. & Lansbury, P. T., Jr. The carboxy terminus of the beta amyloid protein is critical for the seeding of amyloid formation: implications for the pathogenesis of Alzheimer's disease. *Biochemistry* **32,** 4693–4697 (1993).
11. Burdick, D. *et al.* Assembly and aggregation properties of synthetic Alzheimer's A4/beta amyloid peptide analogs. *J. Biol. Chem.* **267,** 546–554 (1992).
12. Riek, R., Guntert, P., Dobeli, H., Wipf, B. & Wuthrich, K. NMR studies in aqueous solution fail to identify significant conformational differences between the monomeric forms of two Alzheimer peptides with widely different plaque-competence, A beta(1-40)(ox) and A beta(1-42)(ox). *Eur. J. Biochem.* **268,** 5930–5936 (2001).
13. Luhrs, T. *et al.* 3D structure of Alzheimer's amyloid-beta(1-42) fibrils. *Proc. Natl. Acad. Sci. USA* **102,** 17342–17347 (2005).
14. Petkova, A. T. *et al.* A structural model for Alzheimer's beta -amyloid fibrils based on experimental constraints from solid state NMR. *Proc. Natl. Acad. Sci. USA* **99,** 16742–16747 (2002).
15. Paravastu, A. K., Leapman, R. D., Yau, W. M. & Tycko, R. Molecular structural basis for polymorphism in Alzheimer's beta-amyloid fibrils. *Proc. Natl. Acad. Sci. USA* **105,** 18349–18354 (2008).
16. Schmidt, M. *et al.* Comparison of Alzheimer Abeta(1-40) and Abeta(1-42) amyloid fibrils reveals similar protofilament structures. *Proc. Natl. Acad. Sci. USA* **106,** 19813–19818 (2009).
17. Colletier, J. P. *et al.* Molecular basis for amyloid-beta polymorphism. *Proc. Natl. Acad. Sci. USA* **108,** 16938–16943 (2011).
18. Eisenberg, D. & Jucker, M. The amyloid state of proteins in human diseases. *Cell* **148,** 1188–1203 (2012).
19. Sawaya, M. R. *et al.* Atomic structures of amyloid cross-[bgr] spines reveal varied steric zippers. *Nature* **447,** 453–457 (2007).
20. Colletier, J. P. *et al.* Amyloid Fibril Models: coordinates and illustrations, http://people.mbi.ucla.edu/sawaya/jmol/fibrilmodels/. (Accessed: 2nd Feb. 2015)
21. Yan, Y. & Wang, C. Abeta42 is more rigid than Abeta40 at the C terminus: implications for Abeta aggregation and toxicity. *J. Mol. Biol* **364,** 853–862 (2006).
22. Bernstein, S. L. *et al.* Amyloid beta-protein: monomer structure and early aggregation states of Abeta42 and its Pro19 alloform. *J. Am. Chem. Soc.* **127,** 2075–2084 (2005).
23. Jarvet, J., Damberg, P., Bodell, K., Göran Eriksson, L. E. & Gräslund, A. Reversible Random Coil to β-Sheet Transition and the Early Stage of Aggregation of the Aβ(12−28) Fragment from the Alzheimer Peptide. *J. Am. Chem. Soc.* **122,** 4261–4268 (2000).
24. Zhang, S. *et al.* The Alzheimer's peptide a beta adopts a collapsed coil structure in water. *J. Struct. Biol.* **130,** 130–141 (2000).
25. Hou, L. *et al.* Solution NMR studies of the A beta(1-40) and A beta(1-42) peptides establish that the Met35 oxidation state affects the mechanism of amyloid formation. *J. Am. Chem. Soc.* **126,** 1992–2005 (2004).
26. Baumketner, A. *et al.* Structure of the 21-30 fragment of amyloid beta-protein. *Protein Sci.* **15,** 1239–1247 (2006).
27. Lim, K. H., Collver, H. H., Le, Y. T., Nagchowdhuri, P. & Kenney, J. M. Characterizations of distinct amyloidogenic conformations of the Abeta (1-40) and (1-42) peptides. *Biochem. Biophys. Res. Commun.* **353,** 443–449 (2007).
28. Lazo, N. D., Grant, M. A., Condron, M. C., Rigby, A. C. & Teplow, D. B. On the nucleation of amyloid beta-protein monomer folding. *Protein Sci.* **14,** 1581–1596 (2005).
29. Coles, M., Bicknell, W., Watson, A. A., Fairlie, D. P. & Craik, D. J. Solution structure of amyloid beta-peptide(1-40) in a water-micelle environment. Is the membrane-spanning domain where we think it is? *Biochemistry* **37,** 11064–11077 (1998).
30. Ball, K. A., Phillips, A. H., Wemmer, D. E. & Head-Gordon, T. Differences in beta-strand Populations of Monomeric Abeta40 and Abeta42. *Biophys. J.* **104,** 2714–2724 (2013).

31. Flock, D., Colacino, S., Colombo, G. & Di Nola, A. Misfolding of the amyloid beta-protein: a molecular dynamics study. *Proteins* **62,** 183–192 (2006).
32. Tomaselli, S. *et al.* The alpha-to-beta conformational transition of Alzheimer's Abeta-(1-42) peptide in aqueous media is reversible: a step by step conformational analysis suggests the location of beta conformation seeding. *Chembiochem* **7,** 257–267 (2006).
33. Vitalis, A. & Caflisch, A. Micelle-Like Architecture of the Monomer Ensemble of Alzheimer's Amyloid-β Peptide in Aqueous Solution and Its Implications for Aβ Aggregation. *J. Mol. Biol.* **403,** 148–165 (2010).
34. Sgourakis, N. G., Yan, Y., McCallum, S. A., Wang, C. & Garcia, A. E. The Alzheimer's peptides Abeta40 and 42 adopt distinct conformations in water: a combined MD/NMR study. *J Mol Biol* **368,** 1448–1457 (2007).
35. Sgourakis, N. G. *et al.* Atomic-level characterization of the ensemble of the Aβ (1–42) monomer in water using unbiased molecular dynamics simulations and spectral algorithms. *J. Mol. Biol.* **405,** 570–583 (2011).
36. Lin, Y. S., Bowman, G. R., Beauchamp, K. A. & Pande, V. S. Investigating how peptide length and a pathogenic mutation modify the structural ensemble of amyloid beta monomer. *Biophys J* **102,** 315–324 (2012).
37. Fezoui, Y. & Teplow, D. B. Kinetic studies of amyloid beta-protein fibril assembly. Differential effects of alpha-helix stabilization. *J. Biol. Chem.* **277,** 36948–36954 (2002).
38. Best, R. B., Buchete, N.-V. & Hummer, G. Are Current Molecular Dynamics Force Fields too Helical? *Biophys. J.* **95,** L07–L09 (2008).
39. Yan, Y., McCallum, S. A. & Wang, C. M35 oxidation induces Abeta40-like structural and dynamical changes in Abeta42. *J. Am. Chem. Soc.* **130,** 5394–5395 (2008).
40. Zweckstetter, M. & Bax, A. Prediction of sterically induced alignment in a dilute liquid crystalline phase: aid to protein structure determination by NMR. *J. Am. Chem. Soc.* **122,** 3791–3792 (2000).
41. Kabsch, W., S. C. Dictionary of protein secondary structure: pattern recognition of hydrogen-bonded and geometrical features. *Biopolymers* **22,** 2577–2637 (1983).
42. Ono, K., Condron, M. M. & Teplow, D. B. Structure-neurotoxicity relationships of amyloid beta-protein oligomers. *Proc. Natl. Acad. Sci. USA* **106,** 14745–14750 (2009).
43. Danielsson, J., Jarvet, J., Damberg, P. & Graslund, A. The Alzheimer beta-peptide shows temperature-dependent transitions between left-handed 3-helix, beta-strand and random coil secondary structures. *FEBS J.* **272,** 3938–3949 (2005).
44. Hoyer, W., Gronwall, C., Jonsson, A., Stahl, S. & Hard, T. Stabilization of a beta-hairpin in monomeric Alzheimer's amyloid-beta peptide inhibits amyloid formation. *Proc. Natl. Acad. Sci. USA* **105,** 5099–5104 (2008).
45. Ahmed, M. *et al.* Structural conversion of neurotoxic amyloid-beta(1-42) oligomers to fibrils. *Nat. Struct. Mol. Biol.* **17,** 561–567 (2010).
46. Ball, K. A. *et al.* Homogeneous and heterogeneous tertiary structure ensembles of amyloid-beta peptides. *Biochemistry* **50,** 7612–7628 (2011).
47. Rosenman, D. J., Connors, C. R., Chen, W., Wang, C. & García, A. E. Aβ Monomers Transiently Sample Oligomer and Fibril-Like Configurations: Ensemble Characterization Using a Combined MD/NMR Approach. *J. Mol. Biol.* **425,** 3338–3359 (2013).
48. Fawzi, N. L. *et al.* Structure and dynamics of the Abeta(21-30) peptide from the interplay of NMR experiments and molecular simulations. *J. Am. Chem. Soc.* **130,** 6145–6158 (2008).
49. Xue, W.-F., Homans, S. W. & Radford, S. E. Systematic analysis of nucleation-dependent polymerization reveals new insights into the mechanism of amyloid self-assembly. *Proc. Natl. Acad. Sci. USA* **105,** 8926–8931 (2008).
50. Paravastu, A. K., Qahwash, I., Leapman, R. D., Meredith, S. C. & Tycko, R. Seeded growth of beta-amyloid fibrils from Alzheimer's brain-derived fibrils produces a distinct fibril structure. *Proc. Natl. Acad. Sci. USA* **106,** 7443–7448 (2009).
51. Cerf, E. *et al.* Antiparallel beta-sheet: a signature structure of the oligomeric amyloid beta-peptide. *Biochem. J.* **421,** 415–423 (2009).
52. Wu, J. W. *et al.* Fibrillar oligomers nucleate the oligomerization of monomeric amyloid beta but do not seed fibril formation. *J. Biol. Chem.* **285,** 6071–6079 (2010).
53. Hess, B., Kutzner, C., van der Spoel, D. & Lindahl, E. GROMACS 4: Algorithms for Highly Efficient, Load-Balanced, and Scalable Molecular Simulation. *J. Chem. Theory Comput.* **4,** 435–447 (2008).
54. Oostenbrink, C., Villa, A., Mark, A. E. & van Gunsteren, W. F. A biomolecular force field based on the free enthalpy of hydration and solvation: the GROMOS force-field parameter sets 53A5 and 53A6. *J. Comput. Chem.* **25,** 1656–1676 (2004).
55. Hess, B., Bekker, H., Berendsen, H. J. C. & Fraaije, J. G. E.M. LINCS: A Linear Constraint Solver for Molecular Simulations. *J. Comp. Chem. Phys. Lett* **18,** 1463–1472 (1997).
56. Darden, T., York, D. & Pedersen, L. Particle mesh Ewald: An N· log (N) method for Ewald sums in large systems. *J. Chem. Phys.* **98,** 10089 (1993).
57. Bussi, G., Donadio, D. & Parrinello, M. Canonical sampling through velocity rescaling. *J Chem Phys* **126,** 014101 (2007).
58. Berendsen, H. J. C., Postma, J. P. M., van Gunsteren, W. F., DiNola, A. & Haak, J. R. Molecular dynamics with coupling to an external bath. *J. Chem. Phys.* **81,** 3684–3690 (1984).
59. Karplus, M. & Anderson, D. Valence-Bond Interpretation of Electron-Coupled Nuclear Spin Interactions; Application to Methane. *J. Chem. Phys.* **30,** 6–10 (1959).
60. Vuister, G. W. & Bax, A. Quantitative J correlation: a new approach for measuring homonuclear three-bond J(HNH.alpha.) coupling constants in 15N-enriched proteins. *Journal of the American Chemical Society* **115,** 7772–7777 (1993).
61. Pardi, A., Billeter, M. & Wuthrich, K. Calibration of the angular dependence of the amide proton-C alpha proton coupling constants, 3JHN alpha, in a globular protein. Use of 3JHN alpha for identification of helical secondary structure. *J Mol Biol* **180,** 741–751 (1984).
62. Smith, L. J., Sutcliffe, M. J., Redfield, C. & Dobson, C. M. Analysis of phi and chi 1 torsion angles for hen lysozyme in solution from 1H NMR spin-spin coupling constants. *Biochemistry* **30,** 986–996 (1991).

Acknowledgements

We thank Prof. Chunyu Wang for offering the NMR measurements of J coupling constants and RDCs. This study was supported by the "100 Talents Project" of CAS (to Y.X.), CAS-Novo Nordisk Great Wall Professorship (to Y.X), the National Natural Science Foundation of China (No. 91013010, No. 21172233, No. 81422047 and No. 31150110578), and the National S&T Major Project (No 2012ZX09301001-005). Computational resources were supported by the National Supercomputing Center in Tianjin (Tianhe-1) and the Computer Network Information Center (CNIC) of the Chinese Academy of Sciences (CAS).

Author Contributions

Y.X., W.S., Y.W., J.-P.C. and H.Y. designed the study; W.S. and Y.W. conducted the MD simulations; W.S. analyzed the MD simulations; W.S. wrote the manuscript with inputs from all authors.

Additional Information

Supplementary information accompanies this paper at http://www.nature.com/srep

Competing financial interests: The authors declare no competing financial interests.

How to cite this article: Song, W. *et al.* Varied Probability of Staying Collapsed/Extended at the Conformational Equilibrium of Monomeric $A\beta_{40}$ and $A\beta_{42}$. *Sci. Rep.* **5**, 11024; doi: 10.1038/srep11024 (2015).